Green's functions theory for semiconductor-quantum-well laser spectra

M. F. Pereira, Jr. and K. Henneberger

Fachbereich Physik, Universität Rostock, D-18051 Rostock, Germany

(Received 30 October 1995)

A microscopic approach for the computation of semiconductor quantum well laser power spectra is presented. The theory is based on nonequilibrium Green's function techniques that allow for a consistent description of the coupled photon and carrier system fully quantum mechanically. Many-body effects are included through vertex corrections beyond the random-phase approximation. Band structure engineering is incorporated in the theory as dictated by the coupled band solutions of the Luttinger Hamiltonian. The influence of the detailed cavity-mode structure is accounted for by the photon Green's function. The theory describes the interplay among the various many-body, quantum-confinement, and band structure effects in the gain medium and its action as a laser cavity. Numerical results for the recombination rates, optical response, and laser output power spectra are presented for strained-layer and lattice-matched III-V systems at quasiequilibrium with variable design and material parameters and under different excitation conditions. Active optical switching is demonstrated in specially designed structures. [S0163-1829(96)01123-X]

I. INTRODUCTION

Semiconductor quantum wells provide an interesting opportunity to manipulate complex nonlinear phenomena and to create high-performance lasers.[1] Advanced theoretical techniques are required to keep up with recent progress on the design and fabrication of quantum well (QW) lasers, to understand the wealth of experimental data available, and to predict the effects that will be exploited in future devices.

Regardless of the effective dimensionality of the system and the microscopic mechanisms that give rise to optical gain, the semiconductor must be consistently treated as both a resonator and gain medium. A realistic description of the excited medium, as given in Ref. 2, requires the combination of band structure and many-body effects. The influence of different material parameters, confinement potentials, strain and well widths has been analyzed recently and the last two combined play a major role in the effective curvature of the bands which, in turn, strongly affect the many-body corrections.[3] The approach was based on the steady-state solutions of generalized semiconductor Bloch equations (SBE's), and has two major limitations. First, it can only describe the active medium in the presence of a macroscopic coherent interband polarization. So, if the medium is incoherently excited by carrier injection or if phase-destroying processes like carrier-carrier and carrier-phonon scattering give rise to a fast decay of the interband polarization created, e.g., by a coherent optical pulse, the SBE's cannot be used. Second, from the SBE's, we can directly compute absorption and gain, but not laser emission. On the other hand, nonequilibrium Green's function techniques are able to treat both interacting carriers and photons under the same quantum mechanical footing[4] and give rise to a consistent description of laser emission.[5]

Fully quantum mechanical treatments have been already applied to bulk systems.[5–8] However, the one-dimensional approach used for light propagation has the serious shortcoming that transverse losses in the carrier kinetics cannot be accounted for in a straightforward way. Moreover, the output

spectrum has been related "by hand" to the field-field correlation function $D^<$, which is introduced here in Sec. II. From a first principles analysis, the laser output is derived directly from the Poynting vector. A fully consistent treatment of the problem, i.e., a three-dimensional description of light propagation and the calculation of the output power directly from the Poynting vector has been already given in Ref. 9, and can be generalized to arbitrary geometries.[10]

In this paper, we restrict the analysis to those output intensities, such that spectral hole burning in the gain does not come into play. Therefore, quasiequilibrium can be assumed in the carrier system. This way, any optical losses in the carrier kinetics (including transverse ones) are negligible. A reduction from the three-dimensional problem to a one-dimensional cavity is then possible. Our nonequilibrium Green's function approach incorporates the most relevant band structure and many-body effects and provides a framework for analyzing nonequilibrium configurations.[4] It includes vertex corrections beyond the random-phase approximation (RPA) that extend previous bulk-system approaches[7] to the quasi-two-dimensional coupled band quantum well case.

In the high density regime in which semiconductor lasers operate, and which is described in this paper, the many-body effects manifest as Pauli-blocking, screening, Coulomb enhancement, and band gap renormalization. For screening, we use an extended static single-plasmon-pole model.[3]

The paper is organized as follows. In Sec. II, we summarize the main steps in the derivation of the Green's functions expressions. We start from the basic Hamiltonian for the system, introduce the Green's functions and their Dyson equations. We discuss the quantum well case in detail and present a procedure to reduce the multilayer, spatially dependent polarization functions to averaged quantities, consistently with the electric dipole approximation. We give a step by step derivation of the dielectric tensor and show explicitly the relation between the retarded polarization function and the macroscopic optical response of the medium found typically in semiclassical approaches involving Maxwell's equa-

tions. In Sec. III, we give the connection between the photon Green's function and the output power of a QW laser cavity. We reduce the three-dimensional propagation problem to a quasi-one-dimensional resonator cavity, for which we give expressions for the laser output. In Sec. IV, we present numerical results for different quantum well media and cavity resonator designs. We start analyzing the influence of band coupling on the energy levels and transition matrix elements that appear explicitly in our many-body expressions. We then study the combined influence of strain, quantum confinement, band structure, and many-body effects on the gain spectrum and recombination rates of the active medium. Finally, we discuss how the cavity geometry, combined with the many-body and band structure effects, changes the computed output spectra, and further analyze the possibility of active optical switching in specially engineered structures. We summarize our results briefly in Sec. V.

II. DERIVATION OF THE GREEN'S FUNCTION EXPRESSIONS

In this section, we outline the derivation of the Green's-function expressions describing the active QW medium coupled to photons. The general formalism[11] has been applied to semiconductors in Ref. 4 and is used here to include the influence of quantum-confinement and multiple subband coupling,[3] as well as vertex corrections beyond RPA (Ref. 7) in the polarization function, which is related to carrier generation and recombination rates and optical gain.

A. Hamiltonian and basic definitions

The total Hamiltonian of the system can be decomposed in electronic (el), electron-light-field interaction (I), free-field (F) and external (ext) terms,

$$H = H_{el} + H_I + H_F + H_{ext}, \quad (1a)$$

$$H_{el} = \int \Psi^\dagger(\vec{R}) H_0 \Psi(\vec{R}) d\vec{R} + \frac{1}{2} \int \Psi^\dagger(\vec{R}) \Psi^\dagger(\vec{R'})$$

$$\times V(\vec{R} - \vec{R'}) \Psi(\vec{R'}) \Psi(\vec{R}) d\vec{R} d\vec{R'}, \quad (1b)$$

$$H_I = -\frac{e}{m_0 c} \int \Psi^\dagger(\vec{R}) \vec{p}(\vec{R}) \cdot \vec{A}(\vec{R}) \Psi(\vec{R}) d\vec{R}$$

$$= -\frac{1}{c} \int \vec{J}(\vec{R}) \cdot \vec{A}(\vec{R}) d\vec{R}, \quad (1c)$$

$$H_F = \sum_{\lambda, \vec{q}} \hbar \omega_q d^\dagger_{\lambda, \vec{q}} d_{\lambda, \vec{q}}, \quad (1d)$$

$$H_{ext} = \int \left[\rho_{ext}(\vec{R}) \Phi(\vec{R}) - \frac{1}{c} \vec{J}_{ext}(\vec{R}) \cdot \vec{A}(\vec{R}) d\vec{R} \right]. \quad (1e)$$

Here, $\Psi(\vec{R})$ is the electron field operator, $V(\vec{R} - \vec{R'}) = e^2/\epsilon_0 |\vec{R} - \vec{R'}|$ is the instantaneous bare Coulomb interaction between the electrons in the system, and $d_{\lambda, \vec{q}}$ denotes the photon annihilation operator in terms of which the electromagnetic field vector potential $\vec{A}$ is expanded,

$$\vec{A}(\vec{R}) = \sum_{\lambda, \vec{q}} \sqrt{\frac{2\pi\hbar c^2}{\Omega \omega_q}} e^{i\vec{q}\cdot\vec{r}} [d^\dagger_{\lambda \vec{q}} + d_{\lambda - \vec{q}}] \vec{e}_{\lambda \vec{q}}, \quad (2)$$

where we have used the Coulomb gauge and $\vec{e}_{\lambda \vec{q}}$ denotes the standard unitary polarization vector. The particle and current densities are given, respectively, by

$$\rho(\vec{R}) = \Psi^\dagger(\vec{R}) \Psi(\vec{R}),$$

$$\vec{J}(\vec{R}) = \frac{-ie\hbar}{2m_0} \{ \Psi^\dagger(\vec{R}) \nabla \Psi(\vec{R}) - [\nabla \Psi^\dagger(\vec{R})] \Psi(\vec{R}) \}, \quad (3)$$

and the scalar potential is the solution of Poisson's equation,

$$\Phi(\vec{R}) = \int \rho_{tot}(\vec{R'}) V(|\vec{R} - \vec{R'}|) d\vec{R'}, \quad (4)$$

where the total particle density reads $\rho_{tot} = \rho + \rho_{ext}$. The analysis is restricted to one-photon processes within the electric dipole approximation. Hence, only linear terms on the vector potential appear in H_I and H_{ext}. The details of the band structure are included in the formalism through the one-particle QW Hamiltonian H_0. As usual in problems dealing with superlattices and quantum wells, details of the superperiodic potential are averaged and described by effective masses, Luttinger parameters, and a piecewise constant potential giving rise to quantum-confinement effects.[12]

The Green's functions considered in our description of the QW laser problem are $G(1\underline{2})$, $\vec{D}(1\underline{2})$, and $W(1\underline{2})$, which describe, respectively, the carriers, photons, and the screened Coulomb interaction. The one-particle carrier Green's function is given by

$$G(1\underline{2}) = -i/\hbar \langle \Psi(\underline{1}) \Psi^\dagger(\underline{2}) \rangle$$

$$\equiv -i/\hbar \frac{\langle \rho_0 T_C [\Psi(\underline{1}) \Psi^\dagger(\underline{2})] S_C \rangle}{\langle \rho_0 S_C \rangle},$$

$$S_C = T_C \exp\left(i/\hbar \int_C H_{ext}(\underline{t}) d\underline{t} \right). \quad (5)$$

Here, $\underline{1} = \vec{R}_1, t_1$. We use the real-time formalism for nonequilibrium first introduced by Keldysh,[11] in which, through the ordering operator T_C, time runs over a contour C from $-\infty$ to $+\infty$ on a positive branch ($t_1 = t_1^+$) and then back from $+\infty$ to $-\infty$ on a negative branch ($t_1 = t_1^-$).

The transverse photon Green's function[4] and screened potential are defined through functional derivatives. They are given, respectively, by

$$\vec{D}(1\underline{2}) = -\frac{c}{4\pi} \frac{\delta \vec{A}_{eff}(\underline{1})}{\delta \vec{J}_{ext}(\underline{2})},$$

$$W(1\underline{2}) = \frac{\delta \Phi_{eff}(\underline{1})}{\delta \rho_{ext}(\underline{2})}, \quad (6)$$

where $\vec{A}_{eff}(\underline{1}) = \langle \vec{A}(\underline{1}) \rangle$, and $\Phi_{eff}(\underline{1}) = \langle \Phi(\underline{1}) \rangle$. The time evolution of the Green's functions can be cast in compact form as Dyson equations (sum over repeated arguments is assumed)

$$[G_0^{-1}(1\underline{3}) - \Sigma(1\underline{3})]G(\underline{3}2) = \delta(12), \qquad (7a)$$

$$[\vec{D}_0^{-1}(1\underline{3}) - \vec{P}(1\underline{3})]\vec{D}(\underline{3}2) = \vec{\delta}(12), \qquad (7b)$$

$$[W_0^{-1}(1\underline{3}) - p(1\underline{3})]W(\underline{3}2) = \delta(12), \qquad (7c)$$

where Σ, $\vec{P}$, and p are, respectively, the carrier self-energy, the transverse polarization function, and the longitudinal polarization function, while $\vec{\delta}$ is the transverse δ function.[4] The free propagators that appear in Eq. (7) read

$$G_0^{-1}(12) = \left[i\hbar\frac{\partial}{\partial \underline{t}_1} - h_{\text{eff}}(\underline{1})\right]\delta(12), \qquad (8a)$$

$$W_0^{-1}(12) = -\frac{\epsilon_0}{4\pi e^2}\triangle_1\delta(12), \qquad (8b)$$

$$D_0^{-1}(12) = [\triangle_1 - 1/c^2\partial^2/\partial \underline{t}_1^2]\delta(12), \qquad (8c)$$

where ϵ_0 denotes the static dielectric function, and the effective one-particle Hamiltonian in the equation for the free-carrier propagator is

$$h_{\text{eff}}(\underline{1}) = H_0(\underline{1}) + \frac{ei\hbar}{cm_o}\vec{A}_{\text{eff}}(\underline{1})\cdot\nabla(\underline{1}) + \Phi_{\text{eff}}(\underline{1}). \qquad (9)$$

B. Vertex corrections

Functional derivative techniques can be used to cast formal solutions to the Dyson equations in a compact form by means of an iterative scheme. We start by defining longitudinal, γ and transverse, Γ vertex functions,

$$\gamma(1\underline{2}\underline{3}) = \frac{\delta G^{-1}(1\underline{2})}{\delta \Phi_{\text{eff}}(\underline{3})}, \vec{\Gamma}(1\underline{2}\underline{3}) = -\frac{4\pi}{c}\frac{\delta G^{-1}(1\underline{2})}{\delta \vec{A}_{\text{eff}}(\underline{3})}, \qquad (10)$$

in terms of which the carrier self-energy and polarization functions read,

$$\Sigma(1\underline{2}) = -i\hbar G(1\underline{3})W(\underline{4}1)\gamma(\underline{3}\underline{2}\underline{4})$$
$$-i\hbar\vec{\Pi}(1\underline{1}')G(1\underline{3})\vec{D}(\underline{4}1')\vec{\Gamma}(\underline{3}\underline{2}\underline{4})|_{1=1'}, \qquad (11a)$$

$$p(1\underline{2}) = i\hbar G(1\underline{3})G(\underline{4}1)\gamma(\underline{3}\underline{4}\underline{2}), \qquad (11b)$$

$$\vec{P}(1\underline{2}) = i\hbar e\vec{\Pi}(1\underline{1}')G(1\underline{4})\vec{\Gamma}(\underline{4}\underline{5}\underline{2})G(\underline{5}1')|_{1=1'}. \qquad (11c)$$

Substitution into the Dyson equations then give rise to expressions for the vertices,

$$\gamma(1\underline{2}\underline{3}) = -\delta(1\underline{3})\delta(1\underline{2}) + \frac{\delta\Sigma(1\underline{2})}{\delta G(\underline{4}\underline{5})}G(\underline{4}\underline{6})G(\underline{7}\underline{5})\gamma(\underline{6}\underline{7}\underline{3}), \qquad (12a)$$

$$\vec{\Gamma}(1\underline{2}\underline{3}) = -\frac{4\pi e}{c^2}\vec{\Pi}(1\underline{1}')\delta(1\underline{3})\delta(1\underline{2})|_{1=1'}$$
$$+\frac{\delta\Sigma(1\underline{2})}{\delta G(\underline{4}\underline{5})}G(\underline{4}\underline{6})\vec{\Gamma}(\underline{6}\underline{7}\underline{3})G(\underline{7}\underline{5}), \qquad (12b)$$

leading to a closed set of equations, that gives rise to systematic approximations by successive iteration on the self-energy. In our approach, band coupling appears explicitly in the equations through the energy levels and matrix elements of the velocity operator $\vec{\Pi}(1\underline{2}) = [\vec{\Pi}(\underline{1}) + \vec{\Pi}^*(\underline{1})]/2 = \hbar[\nabla(\underline{1}) - \nabla(\underline{2})]/2im_0$. Note that, in the absence of transverse corrections, our iteration scheme reduces to that of Ref. 13. The RPA equations are obtained in the first iteration of Eqs. (11) and (12), with $\Sigma = 0$ and consequently $\gamma(1\underline{2}\underline{3}) = -\delta(1\underline{3})\delta(1\underline{2})$, $\vec{\Gamma}(1\underline{2}\underline{3}) = -4\pi e/c^2\vec{\Pi}(1\underline{1})\delta(1\underline{3})\delta(1\underline{2})$. Substitution of the first order approximation gives the first step beyond RPA for the transverse polarization function,

$$\vec{P}(1\underline{2}) = -\frac{4\pi i\hbar e^2}{c^2}\vec{\Pi}(1\underline{1}')[G(1\underline{2})\vec{\Pi}(\underline{2})G(\underline{2}\underline{1}')$$
$$+i\hbar G(1\underline{3})G(\underline{3}\underline{2})W(\underline{4}\underline{3})\vec{\Pi}(\underline{2})G(\underline{4}\underline{1}')G(\underline{2}\underline{4})]_{1=1'}. \qquad (13)$$

Specifying the branches along the Keldysh contour and introducing the Green's function components in the usual way,[14] the compact Dyson Eq. (7b) splits into an equation for the retarded photon Green's function,

$$[\vec{D}_0^{-1}(13) - \vec{P}^r(13)]\vec{D}^r(32) = \vec{\delta}(12), \qquad (14)$$

and one for the propagators,

$$[\vec{D}_0^{-1}(13) - \vec{P}^r(1,3)]\vec{D}(32) - \vec{P}^{\lessgtr}(13)D^a(32) = 0, \qquad (15)$$

where the carrier recombination rate reads,

$$\vec{P}^<(12) = -\frac{4\pi i\hbar e^2}{c^2}\vec{\Pi}(11')(G^<(12)\vec{\Pi}(2)G^>(21')$$
$$+i\hbar W(43)\{G^<(32)\vec{\Pi}(2)G^>(24)$$
$$\times[G^r(13)G^a(41') + G^r(13)G^>(41')$$
$$+G^<(13)G^a(41')] - G^<(13)G^>(41')$$
$$\times[G^a(32)\vec{\Pi}(2)G^r(24) - G^a(32)\vec{\Pi}(2)G^>(24)$$
$$-G^<(32)\vec{\Pi}(2)G^r(24)]\})_{1=1'}, \qquad (16a)$$

and the carrier generation rate is given by

$$\vec{P}^>(12) = -\frac{4\pi i\hbar e^2}{c^2}\vec{\Pi}(11')(G^>(12)\vec{\Pi}(2)G^<(21')$$
$$+i\hbar W(43)\{G^>(13)G^<(41')$$
$$\times[G^a(32)\vec{\Pi}(2)G^r(24) + G^a(32)\vec{\Pi}(2)G^<(24)$$
$$+G^>(32)\vec{\Pi}(2)G^r(24)] - G^>(32)\vec{\Pi}(2)G^<(24)$$
$$\times[G^r(13)G^a(41') - G^r(13)G^<(41')$$
$$-G^>(13)G^a(41')]\})_{1=1'}. \qquad (16b)$$

Note that there is no summation over the variables that appear on the left-hand side of Eq. (16).

C. The quantum well case

The details of the band structure and quantum confinement are included in the formalism through the solutions of the one-particle QW Hamiltonian H_0. As a matter of fact, the field operators in Eq. (5) should, in general, be expanded in terms of solutions for the Hartree problem, or in other words from the self-consistent solution of the Schrödinger equation for the one-electron Hamiltonian H_0 and the Poisson equation. However, in this paper, we restrict to type-I systems in which the electrons and holes are concentrated in the confining region of the QW layers, with negligible barrier penetration. In this case, the electrostatic band profile deformations give rise to negligible corrections for the optical properties relevant for laser operation and can be disregarded.[15] We can thus use an expansion in terms of operators that create $(a^\dagger_{n,\vec{k}})$ or destruct $(a_{n,\vec{k}})$ eigenstates of H_0,

$$\Psi(\vec{R}) = \sum_{n,\vec{k}} \phi_{n,\vec{k}}(\vec{R}) a_{n,\vec{k}}. \qquad (17)$$

The free-particle term in the electronic Hamiltonian of Eq. (1) has two components, $H_0 = H_c + H_v$. For the materials considered in this paper, the band gap is sufficiently large, such that the conduction band electrons can be described by uncoupled parabolic dispersion relations through H_c. Each subband can thus be labeled by the $m_J = \pm 1/2$ projection of the electron spin σ, a quantization label $j = c_1 c_2 \ldots$, and the in-plane momentum $\vec{k}$. In other words, the simple n label of Eq. (17) is a short abbreviation for $n = \{\sigma j\}$, and will be used whenever possible to simplify the notation. The coupled valence bands are described by the Luttinger Hamiltonian H_v. Each subband is in a mixed state that has heavy $m_J = \pm 3/2$ and light-hole components $m_J = \pm 1/2$. The diagonalization method combines a matrix diagonalization technique[16] with a unitary transformation that reduces the Luttinger Hamiltonian operator matrix to two blocks, which are degenerate for the symmetric QW cases considered here for laser structures.[17] Each of these blocks, up and down, is characterized, respectively, by the label p and thus $n = \{pj\}$, $j = v_1 v_2 \ldots$, $p = \{U, D\}$. In some cases, where compressive strain gives rise to negligible overlap between the heavy- and light-hole states, the dispersion relations become parabolic and p reduces to a single spin label σ. See, for example, the solid lines of Fig. 1, which is explained in more detail in Sec. IV. The eigenstates ϕ_n, are given by

$$\phi_{\sigma j \vec{k}}(\vec{R}) = \frac{1}{S^{1/2}} e^{i\vec{k}\cdot\vec{r}} g_j(z) w_{\sigma j}, \qquad (18a)$$

$$\phi_{p j \vec{k}}(\vec{R}) = \frac{1}{S^{1/2}} e^{i\vec{k}\cdot\vec{r}} [\xi_{H p j \vec{k}}(z) w_{Hp} + \xi_{L p j \vec{k}}(z) w_{Lp}]. \qquad (18b)$$

The position vector is separated into in-plane and growth direction components, $\vec{R} = (\vec{r}, z)$, and the subscripts H, L denote, respectively, the contributions that reduce to heavy- and light-hole terms at $\vec{k} = 0$, where there is no band coupling. The envelope functions $\xi_{L p j \vec{k}}(z)$, $\xi_{H p j \vec{k}}(z)$, and $g_j(z)$ are obtained in the diagonalization of H_0. The lattice-periodic parts w_{Hp}, w_{Lp}, and $w_{\sigma j}$ vary on an atomic scale.
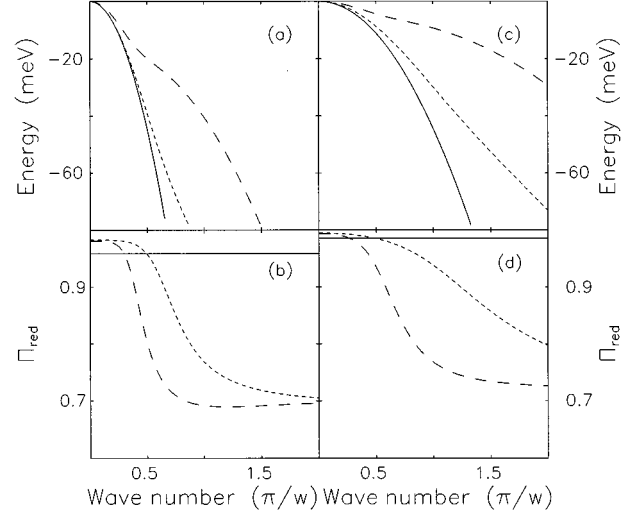

FIG. 1. Free-carrier dispersion relations for the top valence band (a) and velocity matrix element Π_{red} between the top valence and lowest conduction band for the TE-mode polarization (b) of $w = 50$ Å, $In_x Ga_{1-x} As - Al_y Ga_{1-y} As$ quantum wells at $T = 300$ K. For a comparison with a larger well width, we take $w = 100$ Å in (c),(d). In all plots, the compositions of well and barrier layers in the solid, short-dashed, and long-dashed curves correspond, respectively, to $x = 0.15, y = 0$; $x = 0.15, y = 0.3$; $x = 0, y = 0.3$. The origin of energies is taken at $k = 0$.

S is the sample surface and the eigenvalues for the conduction and valence bands are given, respectively, by $\hbar \epsilon^e_{kj} = \hbar \epsilon^e_j + (\hbar^2 k^2 / 2 m^*_e)$ and $\hbar \epsilon^v_{kj}$. Now that our notation has been introduced, we substitute the expansion in Eq. (17) into Eq. (5). Using homogeneity in the plane of the layers, assuming stationary conditions, and considering the Fourier transform upon the relative time difference $t_1 - t_2$, we obtain

$$G(\vec{R}_1, \vec{R}_2, \omega) = \sum_{n_1, n_2, \vec{k}} \phi_{n_1, \vec{k}}(\vec{R}_1) \phi^*_{n_2, \vec{k}}(\vec{R}_2) G_{n_1 n_2}(\vec{k}, \omega). \qquad (19)$$

The interband components of the carrier Green's functions are left out, since they are proportional to the average field, namely, $G_{cv}(\omega) \sim \langle A \rangle$, and within the approach used here[5–10] the mean field is zero. Moreover, nondiagonal intraband terms are neglected, i.e. $G_{n_1 n_2}(\vec{k}, \omega) \sim G_{n_1 n_1}(\vec{k}, \omega) \delta_{n_1 n_2}$, consistently with the approximations used in the computation of Coulomb matrix elements.[3] The first term in Eq. (16) (RPA polarization) is obtained by expanding the Green's functions in eigenstates of the QW states as in Eq. (19). The contribution from a single QW reads

$$i\vec{P}^{\lessgtr}_{\text{QW}}(12) = \frac{4\pi e^2}{c^2} \sum_{n_1 n_2 \vec{k}_1 \vec{k}_2} G^{\lessgtr}_{n_1 n_1}(\vec{k}_1 t_1 t_2) G^{\gtrless}_{n_2 n_2}$$

$$\times \phi_{n_1 \vec{k}_1}(\vec{R}_1) \vec{\Pi}(\vec{R}_1) \phi^*_{n_2 \vec{k}_2}$$

$$\times (\vec{R}_1) \phi^*_{n_2 \vec{k}_2}(\vec{R}_2) \vec{\Pi}(\vec{R}_2) \phi_{n_1 \vec{k}_1}(\vec{R}_2). \qquad (20)$$

The polarization function above has a complicated space dependence that can lead to interesting effects when inserted in the Dyson equation and solved for different structures. However, in our first attempt to analyze the problem, we use the averaged polarization function, or in other words, we treat each quantum well as a homogeneous medium,

$$P_{QW}^{\lessgtr}(12) = \frac{1}{\Omega} \delta(\vec{R}_1 - \vec{R}_2) \int d\vec{R}_3 d\vec{R}_4 \vec{P}_{QW}^{\lessgtr}(\vec{R}_3 \vec{R}_4 t_1 t_2). \quad (21)$$

The spatially local optical response of Eq. (21) is a consequence of the electric dipole approximation, as in bulk systems.[5–8] It is valid whenever the photon momentum is much smaller than the typical carrier momentum. The approximation would break down in the case of coherently coupled multiple quantum wells (MQW's) within a shallow confining potential, allowing for tunneling between adjacent QW's with a large superlattice period $L_p = L_w + L_b$ on the order of a (ultrashort) wavelength. In this paper, we restrict the analysis to isolated MQW systems and optical to near infrared wavelengths, where the approximation holds.

After a Fourier transform in time (stationary systems) and keeping only resonant terms for positive frequencies (rotating wave approximation), the RPA components of the polarization function are

$$iP_{QW,ij}^{\lessgtr}(\omega) = \frac{4\pi e^2/c^2}{\Omega} \sum_{n_1 n_2 \vec{k}_1} G_{n_1 n_1}^{\lessgtr}(\vec{k}_1 \omega)$$

$$\times G_{n_2 n_2}^{\lessgtr}(\vec{k}_1 \omega) \Pi_{n_1 n_2, i}^*(\vec{k}_1) \Pi_{n_1 n_2, j}(\vec{k}_1). \quad (22)$$

We are particularly interested in the diagonal component,

$$iP_{QW,jj}^{\lessgtr}(\omega) = \frac{4\pi e^2/c^2}{\Omega} \sum_{\vec{k}cv\sigma p} |\Pi_{kcv\sigma p,j}|^2 \vartheta_{cv}(k)$$

$$\times \left(\begin{array}{c} f_c^e(k) f_v^h(k) \\ [1 - f_c^e(k)][1 - f_v^h(k)] \end{array} \right), \quad (23)$$

where $\vartheta_{cv}(k)$ is the spectral broadening factor,

$$\vartheta_{cv}(k) = \frac{\hbar \Gamma_{cv}(k)}{[\hbar\omega - \hbar e_{cv}(k)]^2 + \hbar^2 \Gamma_{cv}(k)^2}, \quad (24)$$

$f_c^e(k)$ and $f_v^h(k)$ are the electron and hole distribution functions, and $\Gamma_{cv}(k)$ is the dephasing rate.

The Coulomb corrections beyond the RPA in Eq. (16) within the dipole approximation have the following structure:

$$\vec{P}_{QW}^{\lessgtr}(t_1 t_2) = \frac{4\pi e^2 c^2}{\Omega} \sum_{\lambda} \vec{P}_{\lambda,QW}^{\lessgtr}(t_1 t_2), \quad (25)$$

where the components $\vec{P}_{\lambda,QW}^{\lessgtr}$ have the general form,

$$\vec{P}_{\lambda,QW}^{\lessgtr}(t_1 t_2) = \int d\vec{R}_1 d\vec{R}_2 d\vec{R}_3 d\vec{R}_4 dt_3 dt_4 A(13) \vec{\Pi}(\vec{R}_1) B(41) C(32) \vec{\Pi}(\vec{R}_2) D(24) W(43)$$

$$= \sum_{\substack{n_1 n_2 n_3 n_4 \\ \vec{k}\vec{k}'}} \vec{\Pi}_{n_1 n_2}^*(k) \vec{\Pi}_{n_4 n_3}(k') W\left(\begin{array}{c} n_1 n_2 n_3 n_3 \\ \vec{k}\vec{k}\vec{k}'\vec{k}' \end{array} \right) \int dt_3 dt_4 A_{n_1 n_1}(kt_1 t_3) B_{n_2 n_2}(kt_4 t_1) C_{n_3 n_3}(k't_3 t_2) D_{n_4 n_4}(k't_2 t_4).$$

$$(26)$$

The matrix elements of the screened potential are maximized for $n_3 = n_1, n_2 = n_4$,[3]

$$W\left(\begin{array}{c} n_1 n_2 n_3 n_4 \\ \vec{k}\vec{k}\vec{k}'\vec{k}' \end{array} \right) = \int d\vec{R}_3 d\vec{R}_4 \phi_{n_1 \vec{k}}^*(\vec{R}_3) \phi_{n_2 \vec{k}}(\vec{R}_4) W(\vec{R}_3 \vec{R}_4) \phi_{n_3 \vec{k}'}(\vec{R}_3) \phi_{n_4 \vec{k}'}^*(\vec{R}_4) \approx W_{\vec{k}-\vec{k}'}^{n_1 n_2 n_1 n_2} \delta_{n_1 n_3} \delta_{n_2 n_4}, \quad (27)$$

and again, as in the derivation of Eq. (23), by Fourier transforming with respect to the relative time $t_1 - t_2$, and keeping only resonant terms, we obtain

$$i\vec{P}_{QW}^{\lessgtr}(\omega) = \frac{8\pi e^2/c^2}{\Omega} \sum_{\vec{k}cv\sigma p} \vec{\Pi}_{kcv\sigma p}^* \left[\begin{array}{c} f_c^e(k) f_v^h(k) \\ [1 - f_c^e(k)][1 - f_v^h(k)] \end{array} \right] \vartheta_{cv}(k) [\vec{\Pi}_{kcv\sigma p} + \vec{Y}_{kcv\sigma p}(\omega)], \quad (28)$$

where the Coulomb enhancement factor is given by

$$\vec{Y}_{kcv\sigma p}(\omega) = \sum_{\vec{k}'\sigma' p'} \vec{\Pi}_{k'cv\sigma' p'} W_{\vec{k}-\vec{k}'}^{vcvc} \frac{[\hbar\omega - \hbar e_c(k) - \hbar e_v(k)][1 - f_c^e(k) - f_v^h(k)]}{[\hbar\omega - \hbar e_c(k) - \hbar e_v(k)]^2 + \hbar^2 \Gamma_{cv}(k)^2}. \quad (29)$$

The matrix elements for both bare and screened potential here are simplified by means of the average effective-mass approximation, in which effective dispersion relations giving rise to one average mass per band approximate the band coupling effects. Screening is accounted for through a multisubband extension of the single-plasmon-pole approximation, in which all relevantly populated subbands contribute. In a simple two-band model, the self-energy corrections compensate the change in the chemical potentials that characterize the quasi-equilibrium distributions. However, in the multisubband case considered here, the chemical potentials and self-energies must be computed self-consistently.[3]

The scheme summarized in the preceding paragraph for screening and self-energies has been applied to the computation of nonlinear absorption spectra,[18] in good agreement with experimental results.[19] The results above account for the local response of a single QW. However, we are interested in MQW systems, constituting the active medium in a laser cavity. As a concrete example, we consider an edge emitter configuration with the MQW growth axis along the z direction and a one-dimensional light propagation and emission along the x axis. In a first approximation, we can replace the actual polarization components by the product of a stepwise constant periodic function in z representing the carrier confinement inside the QW layers, and a rectangle function along x to characterize the one-dimensional optical cavity of length L, i.e.,

$$\vec{P}(\vec{R}_1 \vec{R}_2 \omega) = \delta(x_1 - x_2)\delta(y_1 - y_2)\theta(L/2 - |x_1|)\vec{P}^{\lessgtr}_{QW}(\omega)$$

$$\times \sum_i \theta(z_1 + z_{i,L})\theta(z_{i,U} - z_1), \qquad (30)$$

where the lower and upper limits of the ith QW along the z direction are denoted, respectively, by $z_{i,L}$ and $z_{i,U}$. Further, averaging over the growth direction leads to a description of homogeneous excitation inside the sample, i.e.,

$$\vec{P}^{\lessgtr}(\vec{R}_1 \vec{R}_2 \omega) = \delta(\vec{R}_1 - \vec{R}_2)\vec{P}^{\lessgtr}(x_1 \omega), \qquad (31a)$$

$$\vec{P}^{\lessgtr}(x_1 1 \omega) = \theta(L/2 - |x_1|)\left(\frac{L_w}{L_w + L_b}\right)\vec{P}^{\lessgtr}_{QW}(\omega), \quad (31b)$$

where L_w and L_b denote, respectively, the well and barrier lengths. Note that $\vec{P}^r(x_1 \omega)$ can be computed in two steps. The imaginary part follows directly from the relation $2i\text{Im}\vec{P}^r(x_1 \omega) = \vec{P}^>(x_1 \omega) - \vec{P}^<(x_1 \omega)$, and a Kramers-Kronig transformation then yields $\text{Re}\vec{P}^r(x_1 \omega)$. The polarization $\vec{\mathcal{P}}$ that appears in Maxwell's equations is related to the induced current by

$$\vec{J}_{ind}(1) = \frac{\partial \vec{\mathcal{P}}(1)}{\partial t_1}, \qquad (32)$$

and can be expressed as a function of the average electric field $\vec{\mathcal{E}} = -1/c\, \partial \vec{A}_{eff}(1)/\partial t_1$, using the nonlinear optical susceptibility tensor $\vec{\chi}$,

$$\vec{\mathcal{P}}(1) = \int \vec{\chi}^r(13; \vec{\mathcal{E}})\vec{\mathcal{E}}(3)d3. \qquad (33)$$

We thus obtain for the retarded polarization function,

$$\vec{P}^r(12) = -\frac{4\pi}{c^2}\frac{\delta J_{ind}(1)}{\delta \vec{A}_{eff}(2)} = -\frac{4\pi}{c^2}\frac{\partial^2 \vec{\chi}^r(12)}{\partial t_1 \partial t_2}, \qquad (34)$$

where we have used the fact that in our approach $\vec{A}_{eff} = 0$. At steady state, and using Eq. (31), we obtain

$$\vec{P}^r(x_1, \omega) = -4\pi \frac{\omega^2}{c^2}\vec{\chi}^r(x_1, \omega), \qquad (35)$$

or equivalently in terms of the dielectric tensor $\vec{\epsilon}$,

$$\vec{P}^r(x_1, \omega) = \frac{\omega^2}{c^2}[\vec{1} - \vec{\epsilon}(x_1, \omega)]. \qquad (36)$$

III. LASER POWER SPECTRUM

At this point, we can establish a connection between the field-field correlation functions,

$$D^>_{ij}(12) = \frac{1}{4\pi i\hbar}\langle A_i(1)A_j(2)\rangle,$$

$$D^<_{ij}(12) = \frac{1}{4\pi i\hbar}\langle A_j(2)A_i(1)\rangle, \qquad (37)$$

and the power spectrum of a semiconductor QW laser.

A. The one-dimensional resonator

We refer to a concrete device geometry and assume light propagation in the x direction, within an edge emitter configuration for the laser, with TE polarization along the y axis. In other words, $D^{\lessgtr}_{ij}(12) = \delta_{iy}\delta_{jy}D^{\lessgtr}(12)$. Now we proceed to establish a clear connection between the three-dimensional expressions used so far and the one-dimensional treatment that follows. We consider spatial homogeneity in the transverse plane. More details for this case can be found in Ref. 9. Denoting the transverse coordinate and momentum, respectively, by $\vec{\rho}$ and $\vec{q}_\perp$, we have

$$D^<(\vec{R}_1 \vec{R}_2 \omega) = D^<(x_1 x_2, \vec{\rho}_1 \vec{\rho}_2, \omega)$$

$$= \frac{1}{(2\pi)^2}\int d\vec{q}_\perp D^<(x_1 x_2, \vec{q}_\perp, \omega)e^{i\vec{q}_\perp \cdot (\vec{\rho}_1 - \vec{\rho}_2)}, \qquad (38)$$

and consequently,

$$D^<(\vec{R}_1 \vec{R}_2 \omega)|_{\vec{\rho}_1 = \vec{\rho}_2} = D^<(x_1 x_2, \omega)$$

$$= \frac{1}{(2\pi)^2}\int d\vec{q}_\perp D^<(x_1 x_2, \vec{q}_\perp, \omega). \qquad (39)$$

For each frequency, we select those wave numbers that describe propagation along the x direction with a small opening angle θ, i.e., $q_\perp = q_x \tan\theta$. Furthermore, outside the cavity, the optical field is free and then $q_x = \omega/c$. Therefore,

$$D^<(x_1 x_2, \omega) \approx \frac{1}{4\pi} \left(\frac{\omega}{c} \tan\theta \right)^2 D^<(x_1 x_2, \vec{q}_\perp = 0, \omega), \qquad (40)$$

Now from the Dyson equations for the photon Green's functions, Eqs. (14) and (15), and expressing the retarded polarization function in terms of the dielectric tensor of Eq. (36), two equations follow:

$$\left[\Delta + \frac{\omega^2}{c^2} \epsilon_{yy}(x, \omega) \right] D^r(\vec{R}_1 \vec{R}_2 \omega) = \delta_{T,yy}(\vec{R}_1 - \vec{R}_2), \qquad (41a)$$

$$\left[\Delta + \frac{\omega^2}{c^2} \epsilon_{yy}(x, \omega) \right] D^<(\vec{R}_1 \vec{R}_2 \omega) = P^<(x_1 \omega) D^a(\vec{R}_1 \vec{R}_2 \omega). \qquad (41b)$$

Consistently with the discussion above, we consider homogeneity in the transverse direction and keep only the $\vec{q}_\perp = 0$ component after Fourier transforming with respect to the relative transverse coordinate $\vec{\rho}_1 - \vec{\rho}_2$. Using the relation $\delta_{T,yy}(x_1 - x_2, q_\perp = 0) = \delta(x_1 - x_2)$, and dropping the, by now unnecessary, argument $q_\perp = 0$, we obtain the one-dimensional Dyson equations,

$$\left[\Delta + \frac{\omega^2}{c^2} n^2(\omega, x) \right] D^r(x_1 x_2 \omega) = \delta(x_1 - x_2), \qquad (42)$$

for the retarded photon Green's function and accordingly for the propagator,

$$\left[\Delta + \frac{\omega^2}{c^2} n^2(\omega, x) \right] D^<(x_1 x_2 \omega) = P^<(x_1 \omega) D^a(x_1 x_2 \omega), \qquad (43)$$

where we have introduced the refractive index function $n^2(x_1, \omega) = \epsilon_{yy}(x_1, \omega)$. Combining Eqs. (42) and (43), the photon propagator reads,

$$D^<(x_1 x_2 \omega) = \int D^r(x_1 x_3 \omega) P^<(x_3 \omega) D^a(x_3 x_2 \omega) dx_3, \qquad (44)$$

and for the homogeneous excitation inside the sample described by Eq. (31), we get

$$D^<(x_1 x_2 \omega) = P^<(\omega) \int_{-L/2}^{L/2} D^r(x_1 x_3 \omega) D^r(x_2 x_3 \omega)^* dx_3, \qquad (45)$$

where we have used the relation $D^a(x_3 x_2 \omega) = D^r(x_2 x_3 \omega)^*$. We need now an explicit expression for the retarded photon Green's function. Following Ref. 9, we start from the homogeneous equation,

$$\left[\Delta + \frac{\omega^2}{c^2} n^2(\omega, x) \right] F(x) = 0. \qquad (46)$$

There are two regions to be considered, namely, inside and outside the resonator, characterized, respectively, by $|x| < L/2$ and $|x| > L/2$, and two independent plane wave solutions, namely, the forward wave $F(x)$, which strikes the resonator from left to right and the backward wave $B(x) = F(-x)$ that strikes the resonator from right to left,

$$F(x) = B(-x) = \begin{cases} F_+ e^{iq_0 x} + F_- e^{-iq_0 x}, & x < -L/2 \\ f_+ e^{iqx} + f_- e^{-iqx}, & |x| < L/2 \\ G_+ e^{iq_0 x}, & x > L/2. \end{cases} \qquad (47)$$

The general solution to Eq. (46) is constructed from the solutions of the homogeneous equation,

$$D^r(xx'\omega) = \theta(x - x') F(x) B(x') + \theta(x' - x) F(x') B(x). \qquad (48)$$

The coefficients are determined through the usual boundary conditions on the homogeneous equation and by the condition imposed due to the the inhomogeneity, namely, $F'(x) B(x) - B'(x) F(x) = 1$,

$$F_+ = \sqrt{\frac{1 - r^2}{2iq}} \frac{q + q_0}{2q_0} e^{-i(q - q_0)L/2}, \qquad (49a)$$

$$F_- = \sqrt{\frac{r}{(1 - r^2)(2iq)}} \frac{q + q_0}{2q_0} (e^{iqL} - e^{-iqL}) e^{-i(q + q_0)L/2}, \qquad (49b)$$

$$f_- = \frac{r}{\sqrt{(1 - r^2)(2iq)}}, \qquad (49c)$$

$$f_+ = \frac{1}{\sqrt{(1 - r^2)(2iq)}}, \qquad (49d)$$

$$G_+ = \frac{1}{\sqrt{(1 - r^2)(2iq)}} \frac{2q_0}{q + q_0} e^{i(q - q_0)L/2}, \qquad (49e)$$

where the parameters r, q, and q_0 are

$$r = \frac{q - q_0}{q + q_0} e^{iqL}, \quad q = q_1 + iq_2 = q_0 n(\omega), \quad q_0 = \frac{\omega}{c}. \qquad (50)$$

B. The Poynting vector

The light intensity at a given point in space is given by the quantum-statistical average of the Poynting vector,

$$\langle \vec{S}(1) \rangle = \frac{c}{8\pi} \langle \vec{E}(1) \times \vec{B}(2) - \vec{B}(2) \times \vec{E}(1) \rangle_{1=2}. \qquad (51)$$

Using the relations between the vector potential $\vec{A}$ and the electromagnetic fields, $\vec{B} = \nabla \times \vec{A}$ and $\vec{E}(1) = -1/c \, \partial \vec{A}(1)/\partial t_1$, together with Eq. (37), the components of the Poynting vector read,

$$\langle S_i(1) \rangle = \frac{i\hbar}{2} \frac{\partial}{\partial t_1} \sum_{j \neq i} \{ \nabla_j(2) [D_{ji}^>(12) + D_{ji}^<(12)]$$
$$- \nabla_i(2) [D_{jj}^>(12) + D_{ij}^<(12)] \}_{1=2}. \qquad (52)$$

For the linearly polarized light considered here, the expression above reduces to

$$\langle S_x(R_1)\rangle = -\frac{1}{4\pi}\int_{-\infty}^{\infty}d\omega\,\hbar\omega\frac{\partial}{\partial x_1}\{D^<(\vec{R}_1\vec{R}_2\omega)$$

$$+D^>(\vec{R}_2\vec{R}_1\omega)\}|_{1=2}, \tag{53}$$

where we have assumed steady-state conditions and Fourier transformed with respect to the relative time t_1-t_2. Using the relations, $D^{\lessgtr}(\vec{R}_1\vec{R}_2-\omega)=D^{\gtrless}(\vec{R}_2\vec{R}_1\omega)$, we can equivalently write,

$$\langle S_x(\vec{R}_1)\rangle = \int_0^{\infty}d\omega\,I(\omega), \tag{54}$$

and the output power spectrum reads,

$$I(\omega)=\frac{\hbar\omega}{4\pi}\frac{\partial}{\partial x_1}\{2[D^<(\vec{R}_1\vec{R}_2\omega)-D^<(\vec{R}_2\vec{R}_1\omega)]$$

$$+\hat{D}(\vec{R}_1\vec{R}_2\omega)-\hat{D}(\vec{R}_2\vec{R}_1\omega)\}|_{\vec{R}_1=\vec{R}_2}, \tag{55}$$

where we have introduced $\hat{D}(\vec{R}_1\vec{R}_2\omega)=D^>(\vec{R}_1\vec{R}_2\omega)-D^<(\vec{R}_1\vec{R}_2\omega)$. In the one-dimensional propagation approximation, we use Eqs. (39) and (40) to obtain

$$I(\omega)=\frac{\hbar\omega^3}{16c^2\pi^2}\tan^2\theta\frac{\partial}{\partial x_1}\{2[D^<(x_1x_2\omega)-D^<(x_2x_1\omega)]$$

$$+\hat{D}(x_1x_2\omega)-\hat{D}(x_2x_1\omega)\}|_{x_1=x_2}. \tag{56}$$

However, using Eq. (48) and $\hat{D}=2i\,\mathrm{Im}D^r$, it follows that $\hat{D}(x_1x_2\omega)=\hat{D}(x_2x_1\omega)$ and we see that the power spectrum depends only on $D^<$,

$$I(\omega)=\frac{\hbar\omega^3}{8c^2\pi^2}\tan^2\theta\frac{\partial}{\partial x_1}\{D^<(x_1x_2\omega)-D^<(x_2x_1\omega)\}|_{x_1=x_2}. \tag{57}$$

We are interested in the emitted intensity outside the cavity, and thus take $x_1=x_2=L^+/2$. Using Eq. (45), we obtain

$$I(\omega)=\frac{\hbar\omega^3}{4\pi^2c^2}\tan^2\theta iP^<(\omega)\mathrm{Im}\left[\int_{-L/2}^{L/2}dx_3\frac{\partial D^r(x_1x_3\omega)}{\partial x_1}\right.$$

$$\left.\times(D^r(x_2x_3\omega))^*\right]_{x_1=x_2=L^+/2}. \tag{58}$$

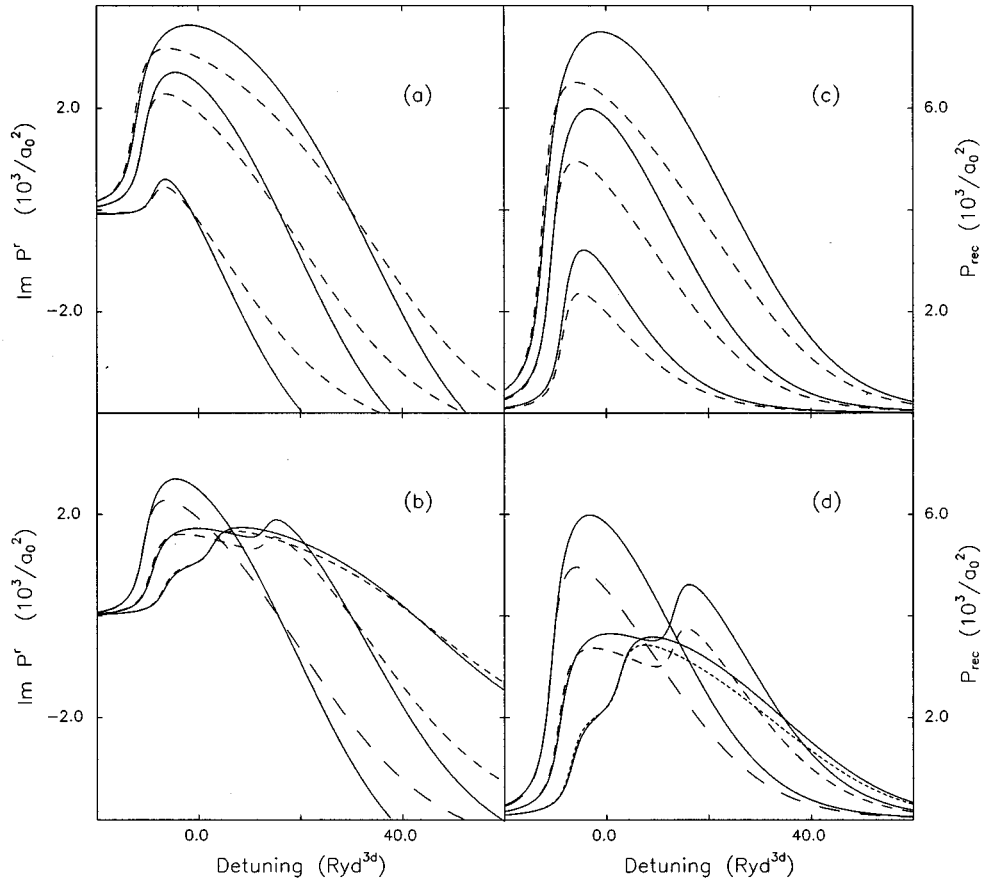The integral in Eq. (58) is easily evaluated, since

FIG. 2. Recombination rate $P_{\mathrm{rec}}(\omega)$ and optical response spectra $\mathrm{Im}P^r(\omega)$ normalized to inverse Bohr radius squared for $\mathrm{In}_{0.15}\mathrm{Ga}_{0.85}\mathrm{As}-\mathrm{GaAs}$ quantum wells at $T=300$ K, as a function of detuning from the free-carrier band gap in 3d Rydbergs. The dashed lines are for RPA, while the solid curves have vertex corrections. (a) $\mathrm{Im}P^r(\omega)$ for a 50 Å quantum well with carrier densities from top to bottom given by $N=6,4,2\times10^{18}$ carriers/cm^3. (b) The carrier density is fixed at $N=4\times10^{18}$ carriers/cm^3, and from top to bottom the well widths are $w=50,100,150$ Å. (c,d) $P_{\mathrm{rec}}(\omega)$ corresponding, respectively, to (a,b).
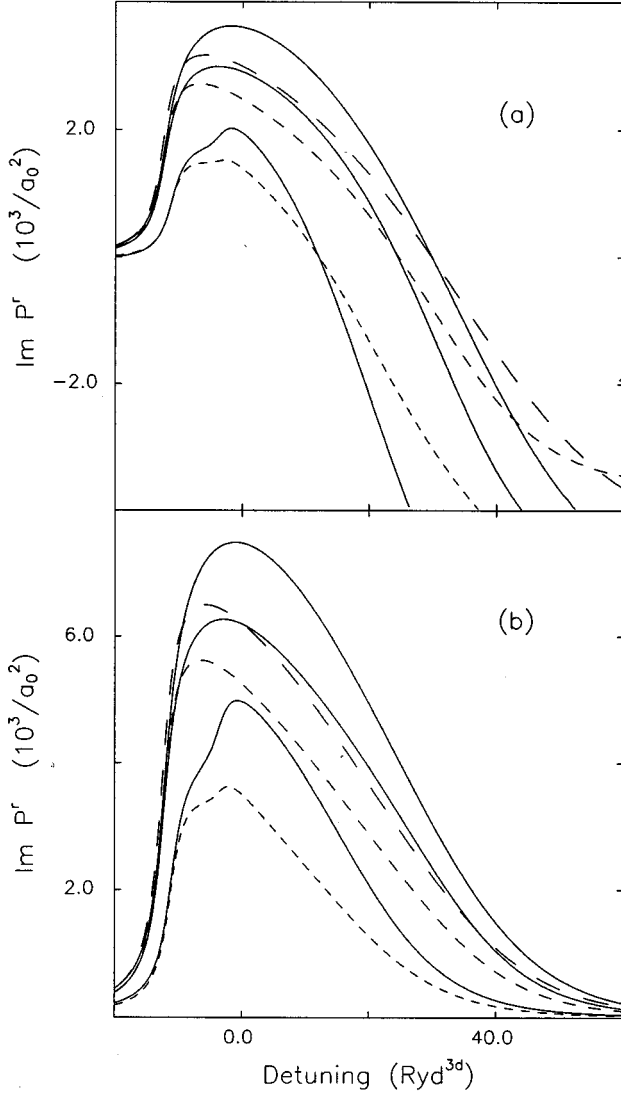
FIG. 3. Optical response spectra $\mathrm{Im}P^r(\omega)$ (a) and recombination rate $P_{\mathrm{rec}}(\omega)$ (b) with the same conventions of Fig. 1 for 50 Å $\mathrm{In}_x\mathrm{Ga}_{1-x}\mathrm{As}-\mathrm{Al}_y\mathrm{Ga}_{1-y}\mathrm{As}$ quantum wells at $T=300$ K and a fixed carrier density of $N=6\times10^{18}$ carriers/cm^3. From top to bottom, the compositions of well and barrier layers are given, respectively, by $x=0.15, y=0; x=0.15, y=0.3; x=0, y=0.3$.

$$\left[\frac{\partial D^r(x_1 x_3 \omega)}{\partial x_1}(D^r(x_2 x_3 \omega))^*\right]_{x_1=x_2=L^+/2}$$

$$=F'(L/2)F^*(L/2)|B(x_3)|^2. \qquad (59)$$

By substitution of the expressions for F and B, we finally obtain for the power spectrum

$$I(\omega)=\frac{\hbar\omega^4}{4\pi^2 c^3}\tan^2\theta i P^<(\omega)L\mathcal{F}_L(\omega), \qquad (60)$$

where the mode structure is described by the cavity function,

$$\mathcal{F}_L(\omega)=\frac{1}{|1-r^2|^2}\frac{1}{|n(\omega)|^2}\frac{1}{|n(\omega)+1|^2}e^{-\omega/cn_2(\omega)L}\mathcal{J}_L(q),$$
$$(61)$$

and the form factor $\mathcal{J}_L(q)$, is a slowly varying function of the cavity length,

$$\mathcal{J}_L(q)=(1+|r|^2)\frac{\sinh(q_2 L)}{q_2 L}+(r^*+r)\frac{\sin(q_1 L)}{q_1 L}. \quad (62)$$

The Fabry-Pérot-like structures in the output spectrum are dominated by the poles in the denominator $1/|1-r^2|^2$ of Eq. (61). Note that Eq. (60) has been derived through quantum-statistical averages of quantized operators, see, e.g., Eqs. (1), (2), (37), and (51). Both stimulated and spontaneous emission are then automatically accounted for in a fully quantum electrodynamical approach.

IV. NUMERICAL RESULTS AND DISCUSSION

In this section, we illustrate the interplay between the quantum-confinement, band structure, and many-body effects on the optical response and recombination rates of the laser medium and the combination of these effects with the cavity-mode structure on the output spectrum. The material parameters used are given in Table I. The band coupling appears explicitly in the equations through the energy levels and matrix elements of the velocity operator $\vec{\Pi}(1\underline{2})=\hbar[\nabla(1)-\nabla(2)]/2im_0$. Within the axial approximation,[12] and taking a root mean square value within the same level of approximation that has been used in Ref. 3 for the electric dipole moment, we get $|\Pi_{kcv\sigma p,j}|^2=(\Pi_{kcv\sigma p})^2$, where

$$\Pi_{kcv\sigma p}=E_{g,0}\langle S|ey|Y\rangle\sqrt{\langle g_c|\xi_{Hpjk}\rangle^2+1/3\langle g_c|\xi_{Lpjk}\rangle^2}, \tag{63}$$

for a TE mode with $\vec{A}=A\hat{y}$ used so far in this paper. Here $E_{g,0}$ is the free-carrier bulk fundamental band gap and $\langle S|ey|Y\rangle$ denotes Kane's dipole matrix element.

Figure 1 shows the top valence band free-carrier dispersion relations and the reduced matrix elements $\Pi_{\mathrm{red}}=\Pi_{kcv\sigma p}/(E_{g,0}\langle S|ex|X\rangle)$ between the top valence and lowest conduction band for the TE-mode polarization of $\mathrm{In}_x\mathrm{Ga}_{1-x}\mathrm{As}\,\mathrm{Al}_y\mathrm{Ga}_{1-y}\mathrm{As}$ quantum wells at $T=300$ K. The origin for the energies is taken at $k=0$. In Figs. 1(a) and 1(b), the well width is $w=50$ Å. For a comparison with a thicker well, we take $w=100$ Å in Figs. 1(c) and 1(d). In all plots, the solid, short-dashed, and long-dashed curves corre-

TABLE I. Material parameters as discussed in Ref. 2. Linear interpolation is used for the alloys. Deformation potentials in eV, lattice parameters in angstroms, and elastic moduli in 10^{11} dyn/cm^2.

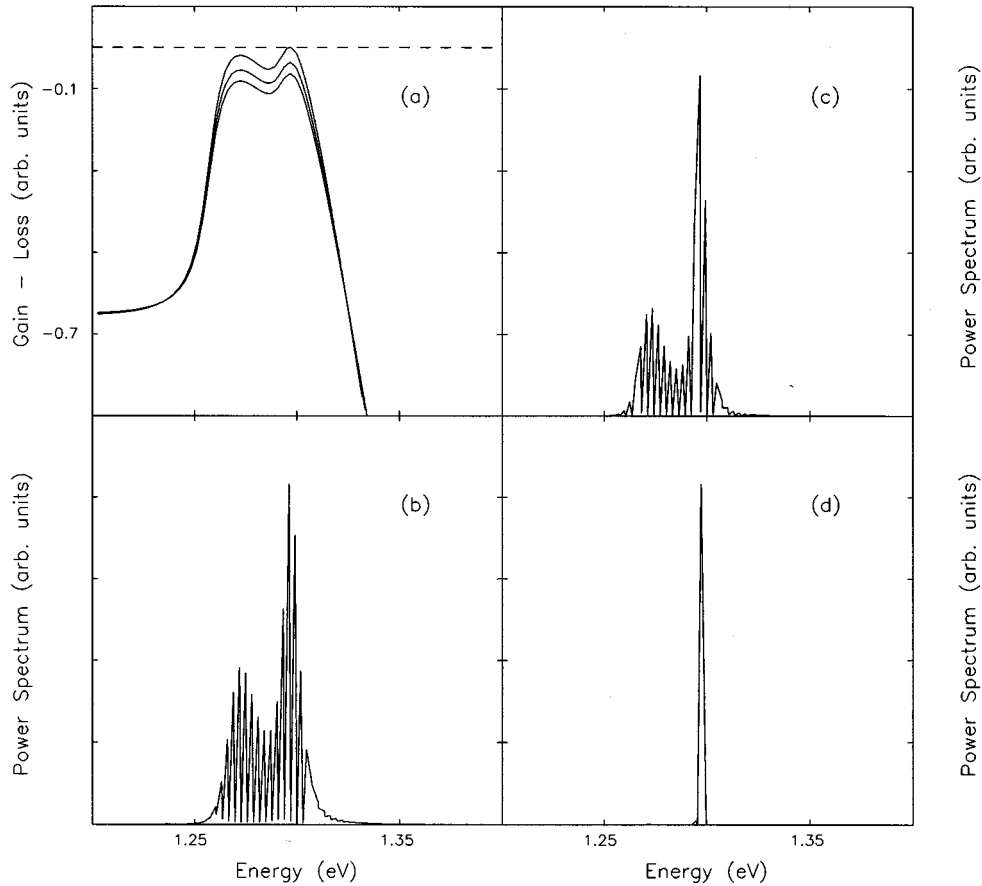| Material	m_c^*	γ_1	γ_2	γ_3	$\epsilon(0)$	$\epsilon(\infty)$	a	b	a_0	C_{11}	C_{12}
GaAs	0.0665	6.79	1.92	2.9	11.78	10.9	7.1	1.7	5.6533	11.88	5.38
InAs	0.027	17.1	7.08	9.29	15.15	12.25	5.9	1.8	6.0583	8.33	4.53

FIG. 4. Normalized *gain-loss* spectrum (a) for 200 Å $In_{0.15}Ga_{0.85}As$-GaAs quantum wells separated by 600 Å barriers at $T = 300$ K and a fixed carrier density of $N = 1.5 \times 10^{18}$ carriers/cm^3. The dashed line marks the gain=loss condition. Each of the solid curves corresponds to a different resonator length L. From bottom to top, the losses decrease by taking, respectively, $L = 60, 63, 67\mu$, and the corresponding output power spectra are shown in (b), (c), and (d). The curves have been normalized, and the actual ratios between the peaks are $I_{max}(63\mu)/I_{max}(60\mu) \approx 3$ and $I_{max}(67\mu)/I_{max}(60\mu) \approx 8238$.

spond, respectively, to the following compositions of well and barrier layers: $x = 0.15, y = 0; x = 0.15, y = 0.3; x = 0, y = 0.3$.

There is no band coupling within our model and for the parameters used here in the $x = 0.15, y = 0$ case. When the barrier is increased, with the addition of aluminum ($x = 0.15, y = 0.3$) the valence bands get coupled, and deviate from parabolicity. Likewise, the reduced velocity matrix element increases at $k = 0$, due to the additional light-hole contributions and experiences a strong k dependence that starts around $k = 0.3$. For the thicker well, the distance between the energy levels is smaller and as such, the band coupling gives rise to stronger deviation from parabolicity for the energies. As expected, the strongest coupling is found for the lattice-matched configuration $x = 0, y = 0.3$.

In all figures below, the dashed lines are for RPA, while the solid curves have vertex corrections as discussed in Sec. II. For simplicity, we use a constant dephasing rate, $\Gamma = \hbar/T_2$, with $T_2 = 100$ fs, and for an easier identification of the computed quantities presented, we refer to $ImP^r(\omega)$ and $P^<(\omega) = P_{rec}(\omega)$, respectively, as the optical response of the inverted semiconductor medium (related to the optical gain), and the (carrier) recombination rate. They are both given in units of the inverse three-dimensional Bohr radius squared.

Figure 2 shows results for $In_{0.15}Ga_{0.85}As$-GaAs quantum wells at $T = 300$ K. The quantum wells are under compressive strain and for the parameters used, the light-hole levels are not bound. Figure 2(a) depicts the optical response for a 50 Å quantum well with carrier densities from top to bottom given by $N = 6, 4, 2 \times 10^{18}$ carriers/cm^3. Figure 2(b), in which the carrier density is fixed at $N = 4 \times 10^{18}$ carriers/cm^3, compares the optical response for different well widths, namely, $w = 50, 100, 150$ Å from top to bottom. For the 50 Å well, the only relevant transition is $E1$-HH1. As the width is increased, the $E2$, HH2 states are also bound and contribute to the gain spectrum. Note that, for increasing carrier density, the spectral position of the peak in the optical response, and consequently of the peak gain, can switch from the lower energy transition $E1$-HH1 to the higher energy $E2$-HH2. Furthermore, the peak separation is reduced for thicker wells.

The stronger electron-hole overlap in the thinner well leads to larger Coulomb interaction and consequently to more significant vertex corrections. In all plots, the band gap renormalization shifts the onset of the optical response to the red. The vertex corrections add to the Pauli blocking and impart a further blueshift to the peak position. Similar considerations can be drawn for the recombination rate of elec-
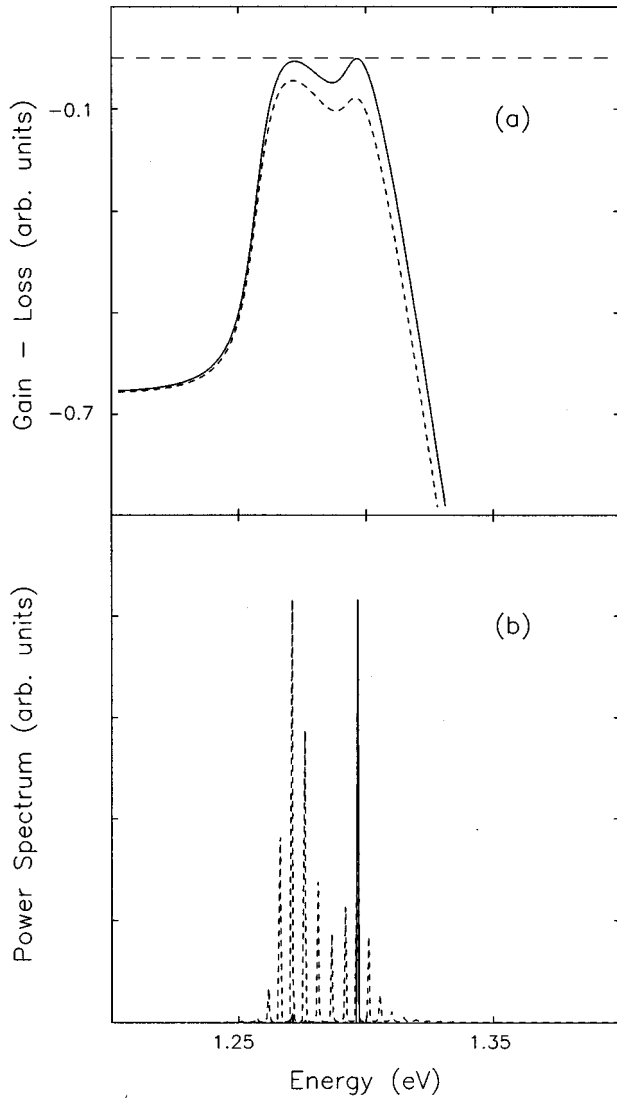
FIG. 5. Normalized *gain-loss* spectrum (a) for 200 Å In$_{0.15}$Ga$_{0.85}$As-GaAs quantum wells separated by 200 Å barriers at $T=300$ K. The long-dashed line marks the gain=loss condition for a 35μ resonator. The short-dashed and solid curves are, respectively, for $N=1.43\times10^{18}$ carriers/cm^3 and $N=1.48\times10^{18}$ carriers/cm^3. The corresponding normalized power spectra are shown in (b). The two curves are normalized, since the peak of the on state is three orders of magnitude larger then that of the off state.

trons and holes in the medium, as shown in Figs. 2(c) and 2(d), which correspond to Figs. 2(a) and 2(b) within the same conventions.

The influence of band coupling on Im$P^r(\omega)$ and $P_{\text{rec}}(\omega)$ can be appreciated, respectively, in Figs. 3(a) and 3(b). The systems selected for these plots are 50 Å In$_x$Ga$_{1-x}$As-Al$_y$Ga$_{1-y}$As, and the carrier density is fixed at $N=6\times10^{18}$ carriers/cm^3. From top to bottom the compositions of well and barrier layers are given, respectively, by $x=0.15, y=0; x=0.15, y=0.3; x=0, y=0.3$. The top curves are thus for uncoupled bands, which are more efficiently inverted and give rise to larger gain and recombination rates. Accordingly, the more efficient occupation of the subbands yields larger band gap shrinkage in excitonic units. As the barrier height is increased through the addition of aluminum

in the middle curves, a light-hole state is bound leading to some band coupling and thus to a reduction of the peak gain and recombination rate values. Finally, the bottom curves are for strongly band-coupled unstrained systems. The peak values are further reduced due to poorer inversion and the second transition, which is a light-hole state at $k=0$, contributes significantly. At the density chosen, it actually determines the peak values of both the recombination rate and gain spectra. Using the results in Sec. III, we can show the connection between the gain spectra and ImP^r. We start by explicitly decomposing the refractive index in real and imaginary parts, $n=n_1+in_2$, and use the fact that for semiconductors $n_1\gg n_2$, to get the relation $n_2\sim -c^2/(2\omega^2\sqrt{\epsilon(\infty)})ImP^r$, where the background dielectric constant $\epsilon(\infty)$ is given in Table I. The usual condition for laser operation, gain = loss can be met only in a limit case in our approach. It corresponds to $|1-r^2|=0$ in the denominator of the cavity function $\mathcal{F}_L(\omega)$ of Eq. (61). From Eq. (50), we can introduce a *gain-loss* function, $G(\omega,L)=-n_2\omega/c-1/L\ln|(n+1)/(n-1)|$.

Figure 4 illustrates the *gain-loss* function for a 200 Å In$_{0.15}$Ga$_{0.85}$As-GaAs quantum well at $T=300$ K and a carrier density of $N=1.5\times10^{18}$ carriers/cm^3. The dashed line marks the gain=loss condition. Each of the solid curves corresponds to a different resonator length L. From bottom to top, the losses decrease by taking, respectively, $L=60,63,67\mu$, and the corresponding output power spectra are given in (b), (c), and (d). The barriers are made three times thicker than the QW widths. Away from the gain = loss condition, several modes are allowed to oscillate, as in Fig. 4(b). As we get closer to the limiting condition, the spectrum increases by several orders of magnitude and the modes closer to the peak gain are favored, as shown in Figs. 4(b) and 4(c). Note, however, that each of the power spectra have been normalized to peak value equal to one for easier visualization. The ratios between the peaks are actually $I_{\text{max}}(63\mu)/I_{\text{max}}(60\mu)\approx3$ and $I_{\text{max}}(67\mu)/I_{\text{max}}(60\mu)\approx8238$.

In Fig. 5 we illustrate the possibility of active optical switching. We use the same QW composition of Fig. 4, but take equal well and barrier widths. The horizontal long-dashed line in Fig. 5(a) marks the *gain=loss* limit for a 35μ resonator. The short-dashed and solid curves are, respectively, for $N=1.43\times10^{18}$ carriers/cm^3 and $N=1.48\times10^{18}$ carriers/cm^3. The corresponding output spectra are shown in Fig. 5(b). The small increase in carrier density switches the peak gain from the lower ($EE1$-HH1) to the upper energy transition ($EE2$-HH2). The peak output switches 26 meV to a higher energy position and increases by a factor of approximately 2136. This clear switching effect is a consequence of engineering the QW energy levels in order to have two well-resolved allowed transitions that yield a camel-back feature in the gain spectrum with two peaks of approximately the same height.

V. SUMMARY

In summary, we have presented a microscopic approach for the computation of multiple quantum well laser output power spectra. The technique is able to describe physical phenomena that require a fully quantized theory for the interaction of radiation and matter in semiconductors and has

the potential for the realistic design and simulation of devices.

We have shown how to formally reduce the three-dimensional problem of an edge emitter laser to an averaged homogeneous medium with quasi-one-dimensional light propagation. Through numerical examples, the optical response and recombination rates were shown to be strongly influenced by a combination of many-body, band coupling, quantum confinement, and strain effects characteristic of actual devices. For thin quantum wells, the stronger electron-hole overlap leads to larger Coulomb interaction and consequently to more significant vertex corrections. Furthermore, as we engineer the structures in order to decouple the valence bands, the more efficient inversion gives rise to larger gain and recombination rates. We have also illustrated how the formalism can be used to predict the output power under the influence of effects, due to manipulations in both the material parameters and resonant cavity design. As expected in an operating laser, away from the gain = loss condition several modes are allowed to oscillate, and as we get closer to the limiting condition, the spectrum increases by several orders of magnitude. Active optical switching has been demonstrated in a specially designed structure with two well-resolved allowed transitions that give rise to a camel-back feature in the gain spectrum with two peaks of approximately the same height. A small increase in carrier density switches the peak gain from the lower (off state) to the upper (on state) energy transition, and the output increases by three orders of magnitude. In reality the total losses increase with carrier density, and that leads to a better spectral resolution of the peak position in the off state. This effect can be automatically included in the formalism by consideration of the emission losses in the carrier kinetics. As a matter of fact, the theory presented here carries the necessary backbone structure for a consistent inclusion of dynamical effects. Departing from Eqs. (7a) and (7b), and using, e.g., a quasi-particle ansatz for the carrier and photon Green's functions,[9] quantum Boltzmann-like equations can be obtained in order to describe transient and nonequilibrium effects in the coupled carrier-photon systems. Proper consideration of the interplay between light emission and carrier-carrier kinetics, as previously analyzed in bulk systems,[20] should be able to describe kinetic holes in the carriers distribution functions leading to spectral holes in the gain spectra, and will be the subject of further investigation. The possibility of tailoring such effects through band structure engineering may give rise to different effects and be of importance for the construction of specific devices. Furthermore, conditions under which spatial inhomogeneities play a significant role and our uniform medium approximation does not hold will also be addressed.

[1] P. Zory, *Quantum Well Lasers* (Academic Press, San Diego, 1993).

[2] M.F. Pereira, Jr., S.W. Koch, and W.W. Chow, Appl. Phys. Lett. **59**, 2941 (1991).

[3] M.F. Pereira, Jr., S.W. Koch, and W.W. Chow, J. Opt. Soc. Am. B **10**, 765 (1993).

[4] K. Henneberger and H. Haug, Phys. Rev. B **38**, 9759 (1988).

[5] K. Henneberger, F. Jahnke, and F. Herzel, Phys. Status Solidi B **173**, 423 (1992).

[6] F. Herzel, K. Henneberger, and W. Vogel, IEEE J. Quantum Electron. **QE-29**, 2891 (1993).

[7] F. Jahnke, K. Henneberger, W. Schaefer, and S.W. Koch, J. Opt. Soc. Am. B **10**, 2394 (1993).

[8] F. Jahnke and S.W. Koch, Phys. Rev. A **52**, 1712 (1995).

[9] K. Henneberger and S.W. Koch, Phys. Rev. Lett. **76**, 1820 (1996).

[10] K. Henneberger (unpublished).

[11] L.V. Keldysh, Zh. Éksp. Teor. Fiz. **47**, 1515 (1964) [Sov. Phys. JETP **20**, 4 (1965)]; in *Instabilities in Semiconductors*, edited by H. Haug (Academic Press, London, 1988).

[12] G. Bastard, *Wave Mechanics of Semiconductor Heterostructures* (Les Editions de Physique, Les Ulis, 1989).

[13] W. Schaefer, in *Optical Nonlinearities and Instabilities in Semiconductors*, edited by H. Haug (Academic Press, San Diego, 1988).

[14] L.P. Kadanoff and G. Baym, *Quantum Statistical Mechanics* (Benjamin, New York, 1962).

[15] R. Binder, I. Galbraith, and S.W. Koch, Phys. Rev. B **44**, 3031 (1991).

[16] J.A. Brum, L.L. Chang, and L. Esaki, Phys. Rev. B **38**, 12 977 (1988).

[17] D.A. Broido and J.L. Sham, Phys. Rev. B **31**, 888 (1985).

[18] M.F. Pereira, Jr., R. Binder, and S.W. Koch, Appl. Phys. Lett. **63**, 279 (1994).

[19] R. Jin, K. Okada, G. Khitrova, H.M. Gibbs, M. Pereira, S.W. Koch, and N. Peyghambarian, Appl. Phys. Lett. **61**, 1745 (1992).

[20] K. Henneberger, F. Herzel, S.W. Koch, R. Binder, A.E. Paul, and D. Scott, Phys. Rev. A **45**, 1853 (1992).